Angle-Multiplexed Metasurfaces: Encoding Independent Wavefronts in a Single Metasurface under Different Illumination Angles

Seyedeh Mahsa Kamali,[1] Ehsan Arbabi,[1] Amir Arbabi,[2] Yu Horie,[1] MohammadSadegh Faraji-Dana,[1] and Andrei Faraon[1,*]

[1]*T.J. Watson Laboratory of Applied Physics and Kavli Nanoscience Institute, California Institute of Technology, 1200 East California Boulevard, Pasadena, California 91125, USA*

[2]*Department of Electrical and Computer Engineering, University of Massachusetts Amherst, 151 Holdsworth Way, Amherst, Massachusetts 01003, USA*

(Received 23 June 2017; published 6 December 2017)

The angular response of thin diffractive optical elements is highly correlated. For example, the angles of incidence and diffraction of a grating are locked through the grating momentum determined by the grating period. Other diffractive devices, including conventional metasurfaces, have a similar angular behavior due to the fixed locations of the Fresnel zone boundaries and the weak angular sensitivity of the meta-atoms. To alter this fundamental property, we introduce *angle-multiplexed metasurfaces*, composed of reflective high-contrast dielectric U-shaped meta-atoms, whose response under illumination from different angles can be controlled independently. This enables flat optical devices that impose different and independent optical transformations when illuminated from different directions, a capability not previously available in diffractive optics.

DOI: 10.1103/PhysRevX.7.041056 Subject Areas: Metamaterials, Optics

I. INTRODUCTION

The concept of angular correlation is schematically depicted in Fig. 1(a) for a diffraction grating. In gratings, the diffraction angle θ_m of order m is related to the incident angle θ_{in} by the relation $d(\sin(\theta_m) - \sin(\theta_{\text{in}})) = m\lambda$, where λ is the wavelength, and d is the grating period, determined solely by the geometry. Therefore, a grating adds a fixed "linear momentum," dictated by its period, to the momentum of the incident light regardless of the incident angle. Similarly, a regular hologram designed to project a certain image when illuminated from a given angle will project the same image (with possible distortions and efficiency reduction) when illuminated from a different angle [Fig. 1(c)]. The concept that we introduce here is shown schematically in Fig. 1(b) for an angle-multiplexed grating that adds a different "linear momentum" depending on the angle of incidence, and in Fig. 1(d) for an angle-multiplexed hologram that displays a different image depending on the angle of incidence. Breaking this fundamental correlation and achieving independent control over distinct incident angles is conceptually new and results in the realization of a new category of compact multifunctional devices that allow for embedding several functions into a thin single metasurface.

*Corresponding author:
A.F:faraon@caltech.edu

Optical metasurfaces are two-dimensional arrangements of a large number of discrete meta-atoms that enable precise control of optical wavefronts with subwavelength resolution [1–13]. Several devices with the ability to control the phase [14–17], polarization [18–20], and amplitude [21–23] of light have been demonstrated. They can directly replace traditional bulk optical components like gratings [24,25], lenses [14,26–28], waveplates [29–31], polarizers [18,32], holograms [33,34], and orbital angular-momentum generators [35,36], or provide novel functionalities [18,29,37–42] that are not feasible with conventional components. For mid-IR to optical wavelengths, high contrast dielectric metasurfaces are very versatile as they can be designed to control different properties of light on a subwavelength resolution and with large reflection or transmission efficiencies [43–56].

Similar to other diffractive devices, metasurfaces that locally control the optical wavefront (e.g., lenses, beam deflectors, holograms) generally have a fixed response when illuminated from different incident angles, with possible distortions and reduction in efficiency at illumination angles other than the design value [37,57,58]. The main reason for this correlated behavior is the constant locations of the Fresnel zone boundaries (i.e., the generalized grating period) that determine the device function irrespective of the incident angle [59,60]. Moreover, almost in all the demonstrated diffractive and metasurface structures, the phase and its local gradient (which is proportional to the local momentum change) have a small dependence on the incident angle [58,61], which results in a large optical memory effect range [62]. Here, we introduce angle-multiplexed metasurfaces for simultaneously encoding of different arbitrary phase profiles in different illumination angles of a single

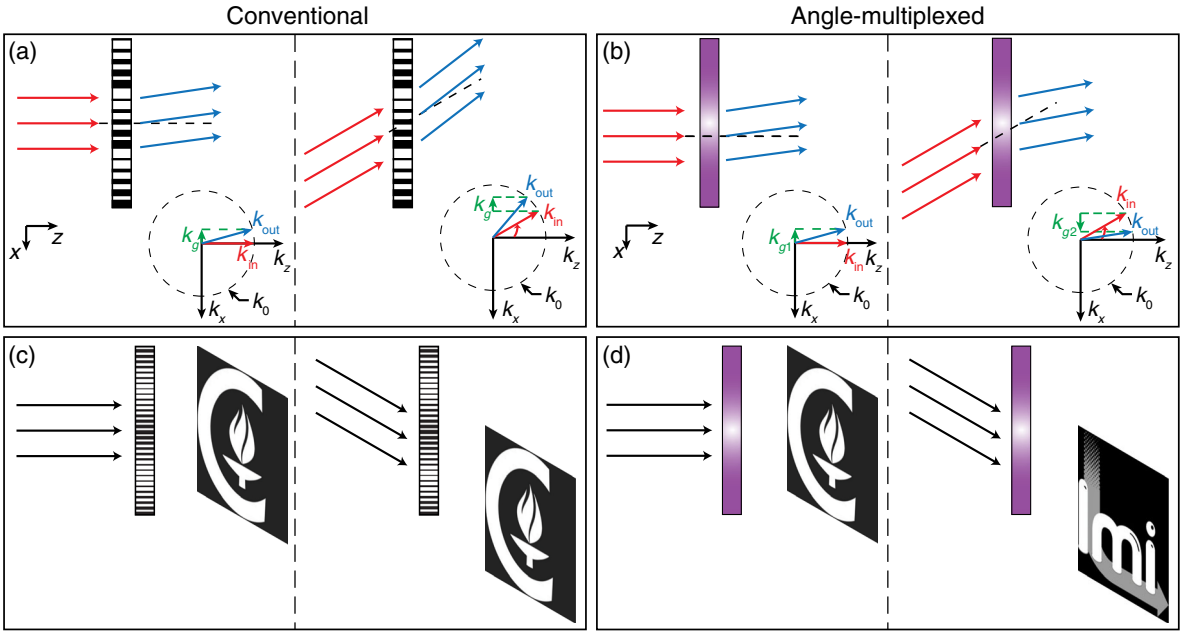

FIG. 1. Angle-multiplexed metasurface concept. (a) Schematic illustration of diffraction of light by a grating. A grating adds a fixed linear momentum ($\hbar k_g$) to the incident light, independent of the illumination angle. If the illumination angle deviates from the designated incident angle, light is deflected to a different angle, which is dictated by the grating period. (b) Illustration of the angle-multiplexed metasurface platform. This platform provides different responses according to the illumination angle. For instance, two gratings with different deflection angles (different grating momenta) can be multiplexed such that different illumination angles acquire different momenta. (c) Illustration of a typical hologram that creates one specific image (Caltech logo) under one illumination angle (left). The same hologram will be translated laterally (and distorted) by tilting the illumination angle (right). (d) Schematic illustration of an angle-multiplexed hologram. Different images are created under different illumination angles. For ease of illustration, the devices are shown in transmission, while the actual fabricated devices are designed to operate in reflection mode.

subwavelength thick metasurface. We introduce a novel angle-dependent platform based on reflective high-contrast dielectric meta-atoms to break the fundamental optical memory effect of metasurfaces and provide independent control over the reflection phase of light at two different incident angles. As a result, any two different functionalities can be embedded in a metasurface that can be separately accessed with different illumination angles. As proof of concept, we experimentally demonstrate angle-multiplexed reflective gratings with different effective grating periods under TE-polarized 0° and 30° illumination angles [Fig. 1(b)]. In addition, we demonstrate an angle-multiplexed hologram, which encodes and projects different holographic images under normal and 30° illumination angles with TE polarization [Fig. 1(d)].

II. OPERATION THEORY AND DESIGN

A meta-atom structure capable of providing independent phase control under TE-polarized light illumination with 0° and 30° incident angles is shown in Fig. 2(a). The amorphous silicon (α-Si) meta-atoms have a U-shaped cross section (we call them U meta-atoms from here on) and are located at the vertices of a periodic square lattice on a low-refractive-index silicon dioxide (SiO_2) and aluminum oxide (Al_2O_3) spacer layers backed by an aluminum reflector. Since the electric field is highly localized in the nanoposts, the low-loss, low-index, dielectric spacer between the nanoposts and the metallic reflector is necessary to avoid the high losses from metal. In addition, the spacer layer allows for efficient excitation of the resonance modes under both angles of illumination through a constructive interference between the incident and reflected fields inside the nanoposts. Therefore, the nanoposts act as one-sided multimode resonators [37–39]. For a wavelength of 915 nm, the meta-atoms are 500 nm tall; the SiO_2 layer, the Al_2O_3 layer, and the aluminum reflector are 125 nm, 30 nm, and 100 nm thick, respectively; and the lattice constant is 450 nm. A uniform array of U meta-atoms provides an angle-dependent response such that TE-polarized light waves incident at 0° and 30° undergo different phase shifts (ϕ_1 and ϕ_2, respectively) as they are reflected from the array. A periodic array of U meta-atoms was simulated to find the reflection amplitude and phase at each incident angle (see Appendix A for simulation details). Any combination of ϕ_1 and ϕ_2 from 0 to 2π can be simultaneously obtained by properly choosing the in-plane dimensions of the meta-atoms [i.e., D_x, D_y, D_{xin}, and D_{yin} as shown in Fig. 2(b)]. Therefore, any two arbitrary and independent phase profiles for TE-polarized 0° and 30° illumination angles can be designed simultaneously (see Appendix A for design procedure details). The corresponding reflection amplitudes ($|r_1|$ and $|r_2|$) and

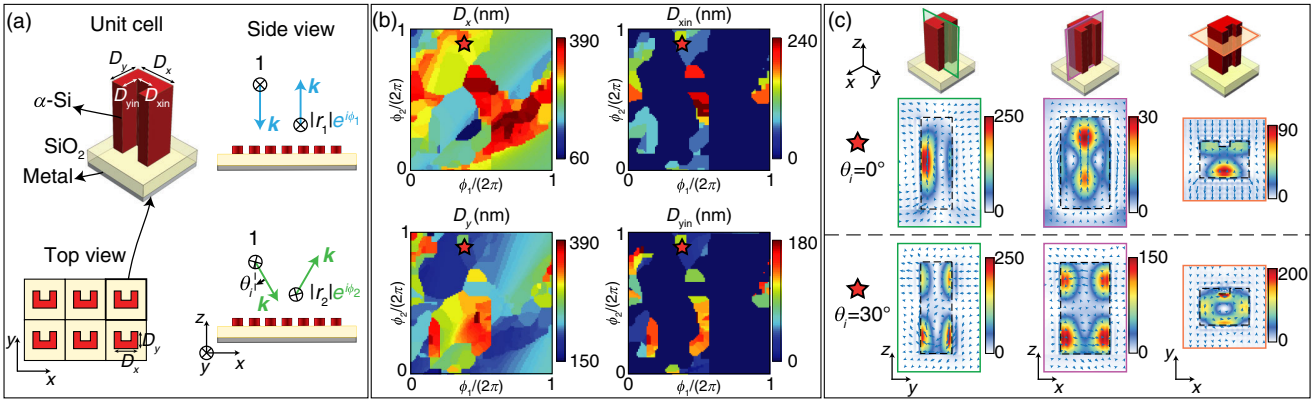

FIG. 2. The meta-atom structure and the design graphs. (a) Schematic drawing of various views of a uniform array of U-shaped cross-section α-Si meta-atoms arranged in a square lattice resting on a thin SiO_2 spacer layer on a reflective surface (i.e., a metallic mirror). The array provides angle-dependent response such that TE-polarized light at 0° and 30° illumination angles undergoes different phase shifts as it reflects from the array. (b) Simulated values of the U meta-atom dimensions (D_x, D_y, D_{xin}, and D_{yin}) for achieving full 2π phase shifts for TE-polarized light at 0° and 30° illumination angles, respectively. From (b), one can find the dimensions of a meta-atom that imposes ϕ_1 and ϕ_2 phase shifts under 0° and 30° illuminations, respectively. (c) Electric energy density inside a single unit cell in a periodic uniform lattice for a typical meta-atom [shown in (b) with a star symbol] at 0° and 30° illumination angles, plotted in three cross sections. Blue arrows indicate in-plane electric field distributions excited at each illumination angle. Different field distributions at normal and 30° incidence are an indication of excitation of different resonant modes under different incident angles. In all parts of the figure, the meta-atoms are 500 nm tall. The silicon dioxide and aluminum layers are 125 nm and 100 nm thick, respectively, the lattice constant is 450 nm, and all simulations are performed at a wavelength of 915 nm. (α-Si: amorphous silicon, SiO_2: silicon dioxide.)

achieved phase shifts are shown in Fig. 1 of Ref. [63]. The independent control of the phase at different incident angles is a result of exciting different modes of the U meta-atom under two distinct illumination angles. Figure 2(c) shows the excited electric energy density for a typical meta-atom in a periodic array at three different cross sections under 0° and 30° incident angles (top and bottom, receptively). The example meta-atom dimensions and corresponding phases at each illumination angle are shown in Fig. 2(b) by a star symbol. Modes that are excited under a 30° illumination angle are different from the excited modes at normal illumination as seen in Fig. 2(c). There are two categories of symmetric and antisymmetric resonant modes. In normal incidence, only symmetric modes are excited, while in oblique illumination, both the symmetric and antisymmetric modes are excited. This is a key factor in realizing this independent control for different angles in a local metasurface platform. As the metasurface is still assumed to be local (i.e., the coupling between adjacent meta-atoms is neglected in the design), any two arbitrary, different wavefronts can be simultaneously designed for the two different illumination angles by using the design graphs shown in Fig. 2(b). In addition, because of the symmetry of the nanoposts (and also as verified from simulation results), the polarization conversion of the metasurface platform from TE to TM is negligible.

III. EXPERIMENTAL RESULTS

The freedom provided by the proposed platform to simultaneously control the phase of light at two distinct incident angles allows for the implementation of a variety of new compact optical components. To demonstrate the versatility of this platform, we fabricated and characterized two examples of angle-multiplexed metasurfaces. First, an angle-multiplexed grating was designed to operate at 0° and 30° incident angles with two different effective grating periods. The angle-multiplexed grating has a diameter of 1 mm and deflects 915-nm TE-polarized light incident at 0° and 30° into −1.85° and +33.2°, respectively. The corresponding effective periods are 31λ (blazed for −1 diffraction order) and 21λ (blazed for +1 diffraction order) for 0° and 30° illuminations, respectively ($\lambda = 915$ nm is the free-space wavelength). The designed devices were fabricated using standard semiconductor fabrication techniques as described in Appendix A. Optical and scanning electron microscope images of the fabricated angle-multiplexed grating are shown in Fig. 3(b). Figure 3(a) shows the measured diffracted light intensities versus angle under 0° (top) and 30° (bottom) TE-polarized illuminations, as well as the simplified measurement setup schematics. The measured reflectance as a function of observation angle shows a dominant peak at the designed angles (i.e., −1.85° under normal illumination and +33.2° under 30° incident angle). Orange dashed lines show deflection angles corresponding to both effective periods, which are 31λ (blazed for −1 diffraction order) and 21λ (blazed for +1 diffraction order). A regular grating with a 31λ period, blazed for −1 diffraction order, would deflect normal incidence into −1.85°, and 30° incident angle into 27.88°. Similarly, another regular grating with a 21λ period, blazed for +1 diffraction order, would deflect normal incidence into +2.7° and 30° incident angle

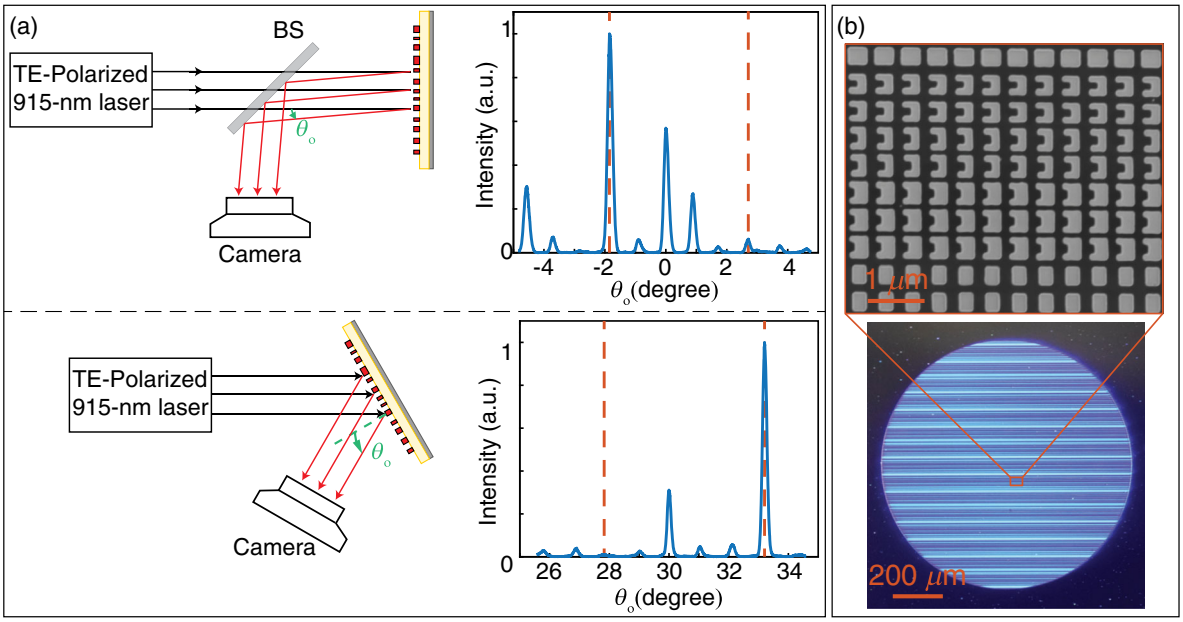

FIG. 3. Angle-multiplexed grating. (a) Simplified schematic of the measurement setup (left) and measured reflectance of the angle-multiplexed grating under normal illumination of TE-polarized light as a function of the observation angle θ_0 (right). The grating deflects 0° and 30° TE-polarized incident light to −1.85° and +33.2°, respectively. Orange dashed lines indicate the designed deflection angles (−1.85° and +33.2° under 0° and 30° incidence, respectively) and the deflection angles corresponding to regular gratings with fixed grating periods (2.7° under normal and 27.88° under 30° illumination angles assuming grating periods of 21λ and 31λ, respectively). See Appendix B and Ref. [63] (Fig. 2) for measurement details. (b) Optical image of the angle-multiplexed grating. The inset shows a scanning electron micrograph of the top view of meta-atoms composing the metasurface. See Appendix B for fabrication details. BS is for beam splitter.

into 33.2°. The angle-multiplexed grating, on the other hand, deflects 0° and 30° incident angles into −1.85° and +33.2°, respectively, with no strong deflection peaks at the angle corresponding to the other grating periods (which are +2.7° and 27.88°). The deflection efficiency of the grating at each incident angle is defined as the power deflected by the grating to the desired order, divided by the power reflected from a plain aluminum reflector (see Appendix B for measurement details and Fig. 2 of Ref. [63] for measurement setups). Deflection efficiencies of 30% and 41% were measured under 0° and 30° incident angles, respectively. For comparison, we simulated the central ∼200-μm-long portion of the grating with a finite-difference time-domain, full-wave electromagnetic solver [64] (see Note 1 and Fig. 3 in Ref. [63] for simulation results). The simulated deflection efficiencies are 63% and 54% for 0° and 30° operation, respectively. To consider the possible fabrication errors, we also simulated the grating with a random error added to all in-plane sizes of the meta-atoms. The error is normally distributed with a zero mean, a 4-nm standard deviation, and a forced maximum of 8 nm. The simulated deflection efficiencies with the added errors are 46% and 39% under 0° and 30° incident angles. We attribute the remaining difference between simulated and measured efficiencies to two factors: First, the deposited aluminum reflected layer has a significant surface roughness. This may result in the existence and excitation of local surface plasmon resonances that contribute to both increased loss and reflection phase error. Second, to counter the effects of systematic fabrication errors, an array of gratings with different biases added to each size of the meta-atoms is fabricated. In the measurements, one of the devices with good performance under both illumination angles is selected and characterized (i.e., there are other fabricated gratings that demonstrate higher efficiencies for one of the angles). As a result, the characterized device might differ from the one with sizes closest to design values. This may justify the different balances between measured and simulated values for efficiencies under the two illumination angles.

As a second example, an angle-multiplexed hologram that projects two different images under 0° and 30° illumination angles was designed, fabricated, and characterized. The hologram covers a 2-mm-by-2-mm square and projects the Caltech and LMI logos when illuminated by TE-polarized light at 915 nm at 0° and 30° incident angles. Optical and scanning electron microscope images of a portion of the fabricated hologram are shown in Fig. 4(b). Simulated and measured intensity profiles for two different illumination angles (top and bottom) are shown in Fig. 4(a), along with simplified schematics of the measurement setups. The Caltech logo is created under normal illumination. By scanning the incident angle from 0° to 30°, the projected image changes from the Caltech logo to the LMI logo. The change in the recorded image with incident angle

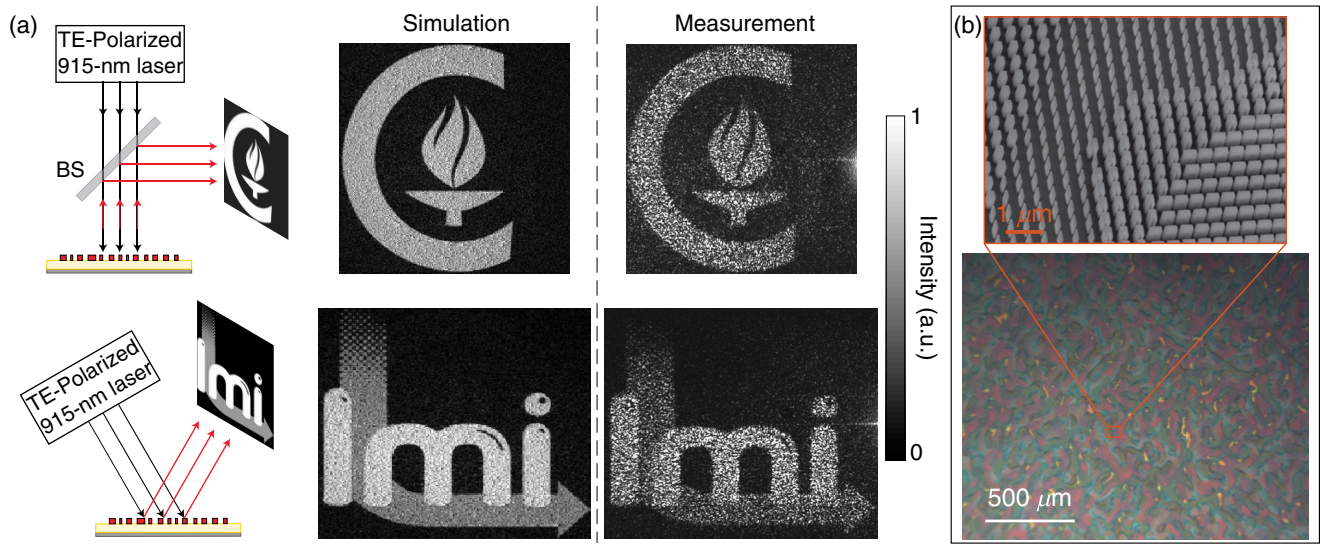

FIG. 4. Angle-multiplexed hologram. (a) Simplified drawing of the measurement setups under normal and 30° illumination angles (left). The angle-multiplexed hologram is designed to create two different images under different incident angles (Caltech and LMI logos under 0° and 30°, respectively). Simulated and measured reflected images captured under 915-nm TE-polarized light at 0° and 30° illumination angles are shown on the right. See Appendix B and Ref. [63] (Fig. 3) for measurement details. (b) Optical image of a portion of the angle-multiplexed hologram. The inset shows a scanning electron micrograph under oblique view of meta-atoms composing the metasurface. See Appendix B for fabrication details.

is shown in Movie 1 in Ref. [63]. The good agreement between the simulation and measurement results confirms the independent control of this platform over distinct incident angles. In order to avoid an overlap between the holographic image and the zeroth-order diffraction, the holograms are designed to operate off axis (see Appendix A for details of hologram design).

IV. DISCUSSION

The angle-multiplexed metasurface platform allows for devices that perform completely independent functions (i.e., grating, lens, hologram, orbital angular-momentum generator, etc.) for different angles of illumination. It is worth noting that the concept and implementation of the angle-multiplexed metasurfaces are fundamentally different from multi-order gratings. While the multi-order gratings can be designed such that the efficiencies of different diffraction orders vary with the incident angle [65,66], the grating momentum corresponding to each order (which is locked to the period of the grating) remains fixed. This difference becomes much clearer when considering the case of holograms. Unlike in the demonstrated platform, it is not possible to encode two completely independent phase profiles corresponding to two completely independent functions in a multi-order holographic optical element (i.e., the generalized case of the multi-order gratings).

V. CONCLUSION

In conclusion, we developed optical metasurfaces that break the angular correlation of thin diffractive components and enable devices where independent phase masks can be embedded in a single thin layer and accessed separately under different illumination angles. Here, the shape of the meta-atom was chosen intuitively, and we expect that by utilizing more advanced optimization procedures, the independent control can be extended to more angles and the device performance can be improved significantly. From a technological point of view, this is a novel class of metasurfaces that opens the path towards ultracompact multifunctional flat devices that are not feasible otherwise. This is complementary to the previously demonstrated independent control over different polarizations [18,67] or wavelengths of the incident light [20,68–70] and thus significantly expands the range of applications for nano-engineered metasurfaces.

ACKNOWLEDGMENTS

This work was supported by the DOE "Light-Material Interactions in Energy Conversion" Energy Frontier Research Center funded by the U.S. Department of Energy, Office of Science, Office of Basic Energy Sciences under Grant No. DE-SC0001293. A. A., E. A., and M. F. were supported by Samsung Electronics. A. A. and Y. H were also supported by DARPA. The device nanofabrication was performed at the Kavli Nanoscience Institute at Caltech.

APPENDIX A: SIMULATION AND DESIGN

To find the reflection amplitude and phase of a uniform array of meta-atoms, the rigorous coupled wave analysis (RCWA) technique was used [71]. A normal and a 30°

incident plane wave at 915 nm wavelength were used as the excitation, and the amplitude and phase of the reflected wave were extracted. The subwavelength lattice for both normal and oblique illumination angles results in the excitation of only the zeroth-order diffracted light. This justifies the use of only one reflection value at each illumination angle for describing the optical behavior of the meta-atom at each illumination angle. The α-Si layer was assumed to be 500 nm thick. The SiO_2 and aluminum layers were assumed to be 125 nm and 100 nm thick, respectively. Refractive indices at 915 nm wavelength were assumed as follows: α-Si: 3.558, SiO_2: 1.44, Al_2O_3: 1.7574, and Al: 1.9183-*i*8.3447. The meta-atom in-plane dimensions (D_x, D_y, $D_{x\mathrm{in}}$, and $D_{y\mathrm{in}}$) are swept such that the minimum feature size remains larger than 50 nm for relieving fabrication constraints.

The optimum meta-atom dimensions for each lattice site at the two incident angles were found by minimizing the total reflection error, which is defined as $\epsilon = |\exp(\mathrm{i}\phi_1) - \mathrm{r}_1|^2 + |\exp(\mathrm{i}\phi_2) - \mathrm{r}_2|^2$, where r_1 and r_2 are the complex reflection coefficients of the unit cell at the two incident angles. Therefore, for any desired combination of phases ϕ_1 and ϕ_2 in the 0 to 2π range at the two incident angles, there is a corresponding meta-atom (i.e., D_x, D_y, $D_{x\mathrm{in}}$, and $D_{y\mathrm{in}}$ values) that minimizes the reflection error. To limit the rapid jumps in dimensions shown in Fig. 2(b), some modification terms were added to the reflection error in order to ensure that adjacent dimensions are preferred for the adjacent phases. The modification terms were defined as an exponential function of the Euclidean distance between the in-plane dimensions of the meta-atoms for adjacent phase values.

The holograms of different incident angles were designed individually using the Gerchberg-Saxton (GS) algorithm with deflection angles of about 3°. The simulation results presented in Fig. 4 were computed by assuming that the coupling among adjacent meta-atoms is negligible, such that each meta-atom imposes the exact complex reflection amplitude found from simulations of the periodic structure. The hologram area was assumed to be illuminated uniformly with 0° and 30° incident-angle plane waves, and the projected holographic images were found by taking the Fourier transform of the field after being reflected from the phase mask.

APPENDIX B: SAMPLE FABRICATION AND MEASUREMENT PROCEDURE

An aluminum layer of about 100 nm was evaporated on a silicon wafer, followed by an Al_2O_3 layer of about 30 nm. A 125-nm-thick SiO_2 and a 500-nm-thick α-Si layer were subsequently deposited using the plasma-enhanced chemical vapor deposition (PECVD) technique at 200 °C. A Vistec EBPG5200 e-beam lithography system was used to define the pattern in a nearly 300-nm-thick layer of ZEP-520A positive electron-beam resist (spin coated at 5000 rpm for 1 min). The pattern was developed in the resist developer (ZED-N50 from Zeon Chemicals) for 3 minutes. A nearly 50-nm-thick Al_2O_3 layer was evaporated on the sample, and the pattern was then transferred to the Al_2O_3 layer by a lift-off process. The patterned Al_2O_3 hard mask was then used to dry etch the α-Si layer in a mixture of SF_6 and C_4F_8 plasma. Finally, the Al_2O_3 mask was removed in a 1:1 solution of ammonium hydroxide and hydrogen peroxide at 80 °C.

The angle-multiplexed grating was measured using the setup shown schematically in Fig. S2 in Ref. [63]. A 915-nm fiber-coupled semiconductor laser was used for illumination, and a fiber collimation package (Thorlabs F220APC-780) was used to collimate the incident beam. A polarizer (Thorlabs LPVIS100-MP2) was inserted to confirm the TE polarization state of the incident light. An additional lens with a focal length of 10 cm (Thorlabs AC254-100-B-ML) was placed before the grating at a distance of about 8 cm to partially focus the beam and reduce the beam divergence after being deflected by the grating in order to decrease the measurement error. The light deflected from the device was imaged using a custom-built microscope. The microscope consists of a 10X objective lens (Mitutoyo M Plan Apo 10X, NA = 0.28) and a tube lens (Thorlabs LB1945-B-ML) with a focal distance of 20 cm, which images the object plane onto a camera (CoolSNAP K4 from Photometrics). A rotation stage was used to adjust the illumination angle, and a 50/50 beam splitter (Thorlabs NIR Non-Polarizing Cube Beamsplitter) was inserted before the grating for measurements under normal illumination. For efficiency measurements of the grating, an iris was used to select the desired diffraction order and block all other diffraction orders. A power meter (Thorlabs PM100D) with a photodetector (Thorlabs S122C) was used to measure the deflected power off the grating, as well as the reflected power from a plain aluminum reflector (from an area adjacent to the grating). The grating efficiency was calculated by dividing the power deflected to the desired order to the power reflected by the aluminum reflector. Neutral density (ND) filters (Thorlabs ND filters, B coated) were used to adjust the light intensity and decrease the background noise captured by the camera.

The angle-multiplexed hologram was characterized using the setup shown schematically in Fig. S3 in Ref. [63]. The setup is similar to the grating measurement setup with some modifications. The 10-cm focal distance lens used to partially focus light to the grating was removed to obtain a relatively uniform illumination of the hologram area. The input beam being larger than the device, in addition to fabrication imperfections, results in a strong zeroth-order diffraction. The zeroth-order diffraction is cropped in Fig. 4(a), as it is outside the holographic image of interest because of the off-axis design of the hologram. The custom-built microscope was also altered as follows: The objective lens was used to generate a Fourier transform of the hologram plane in its back focal plane. The tube lens

was replaced by a lens with a focal length of 6 cm, which images the back focal plane of the objective into the camera. Two rotation stages were used in order to be able to independently rotate the device and the illumination beam. The camera and the imaging setups were not on the rotation stages.

[1] A. V. Kildishev, A. Boltasseva, and V. M. Shalaev, *Planar Photonics with Metasurfaces*, Science **339**, 1232009 (2013).

[2] S. Vo, D. Fattal, W. V. Sorin, Z. Peng, T. Tran, M. Fiorentino, and R. G. Beausoleil, *Sub-wavelength Grating Lenses with a Twist*, IEEE Photonics Technol. Lett. **26**, 1375 (2014).

[3] P. Lalanne, S. Astilean, P. Chavel, E. Cambril, and H. Launois, *Blazed Binary Subwavelength Gratings with Efficiencies Larger than Those of Conventional Échelette Gratings*, Opt. Lett. **23**, 1081 (1998).

[4] S. Astilean, P. Lalanne, P. Chavel, E. Cambril, and H. Launois, *High-efficiency Subwavelength Diffractive Element Patterned in a High-Refractive-Index Material for 633 nm*, Opt. Lett. **23**, 552 (1998).

[5] P. Qiao, W. Yang, and C. J. Chang-Hasnain, *Recent Advances in High-Contrast Metastructures, Metasurfaces and Photonic Crystals*, arXiv:1707.07753.

[6] S. Jahani and Z. Jacob, *All-Dielectric Metamaterials*, Nat. Nanotechnol. **11**, 23 (2016).

[7] I. Staude and J. Schilling, *Metamaterial-Inspired Silicon Nanophotonics*, Nat. Photonics **11**, 274 (2017).

[8] H. H. Hsiao, C. H. Chu, and D. P. Tsai, *Fundamentals and Applications of Metasurfaces*, Small Methods **1**, 1600064 (2017).

[9] P. Genevet, F. Capasso, F. Aieta, M. Khorasaninejad, and R. Devlin, *Recent Advances in Planar Optics: From Plasmonic to Dielectric Metasurfaces*, Optica **4**, 139 (2017).

[10] A. I. Kuznetsov, A. E. Miroshnichenko, M. L. Brongersma, Y. S. Kivshar, and B. Luk'yanchuk, *Optically Resonant Dielectric Nanostructures*, Science **354**, aag2472 (2016).

[11] A. Y. Zhu, A. I. Kuznetsov, B. Luk'yanchuk, N. Engheta, and P. Genevet, *Traditional and Emerging Materials for Optical Metasurfaces*, Nanophotonics **6**, 452 (2017).

[12] F. Ding, A. Pors, and S. I. Bozhevolnyi, *Gradient Metasurfaces: A Review of Fundamentals and Applications*, Rep. Prog. Phys., DOI: 10.1088/1361-6633/aa8732 (2017).

[13] L. Jiang, S. Zeng, Z. Xu, Q. Ouyang, D.-H. Zhang, P. H. J. Chong, P. Coquet, S. He, and K.-T. Yong, *Multifunctional Hyperbolic Nanogroove Metasurface for Submolecular Detection*, Small **13**, 1700600 (2017).

[14] A. Arbabi, Y. Horie, A. J. Ball, M. Bagheri, and A. Faraon, *Subwavelength-Thick Lenses with High Numerical Apertures and Large Efficiency Based on High-Contrast Transmitarrays*, Nat. Commun. **6**, 7069 (2015).

[15] Y. F. Yu, A. Y. Zhu, R. Paniagua-Domínguez, Y. H. Fu, B. Luk'yanchuk, and A. I. Kuznetsov, *High-Transmission Dielectric Metasurface with 2π Phase Control at Visible Wavelengths*, Laser Photonics Rev. **9**, 412 (2015).

[16] K. Chen *et al.*, *A Reconfigurable Active Huygens' Metalens*, Adv. Mater. **29**, 1606422 (2017).

[17] P. K. Jha, X. Ni, C. Wu, Y. Wang, and X. Zhang, *Metasurface-Enabled Remote Quantum Interference*, Phys. Rev. Lett. **115**, 025501 (2015).

[18] A. Arbabi, Y. Horie, M. Bagheri, and A. Faraon, *Dielectric Metasurfaces for Complete Control of Phase and Polarization with Subwavelength Spatial Resolution and High Transmission*, Nat. Nanotechnol. **10**, 937 (2015).

[19] C. Pfeiffer and A. Grbic, *Cascaded Metasurfaces for Complete Phase and Polarization Control*, Appl. Phys. Lett. **102**, 231116 (2013).

[20] E. Arbabi, A. Arbabi, S. M. Kamali, Y. Horie, and A. Faraon, *High Efficiency Double-Wavelength Dielectric Metasurface Lenses with Dichroic Birefringent Metaatoms*, Opt. Express **24**, 18468 (2016).

[21] P. Cencillo-Abad, J.-Y. Ou, E. Plum, and N. I. Zheludev, *Electro-mechanical Light Modulator Based on Controlling the Interaction of Light with a Metasurface*, Sci. Rep. **7**, 5405 (2017).

[22] Y. Zhao, N. Engheta, and A. Al, *Homogenization of Plasmonic Metasurfaces Modeled as Transmission-Line Loads*, Metamaterials **5**, 90 (2011).

[23] K. Thyagarajan, R. Sokhoyan, L. Zornberg, and H. A. Atwater, *Millivolt Modulation of Plasmonic Metasurface Optical Response via Ionic Conductance*, Adv. Mater. **29**, 1701044 (2017).

[24] D. Lin, M. Melli, E. Poliakov, P. St. Hilaire, S. Dhuey, C. Peroz, S. Cabrini, M. Brongersma, and M. Klug, *Optical Metasurfaces for High Angle Steering at Visible Wavelengths*, Sci. Rep. **7**, 2286 (2017).

[25] D. Sell, J. Yang, S. Doshay, R. Yang, and J. A. Fan, *Large-Angle, Multifunctional Metagratings Based on Freeform Multimode Geometries*, Nano Lett. **17**, 3752 (2017).

[26] M. Khorasaninejad, W. T. Chen, R. C. Devlin, J. Oh, A. Y. Zhu, and F. Capasso, *Metalenses at Visible Wavelengths: Diffraction-Limited Focusing and Subwavelength Resolution Imaging*, Science **352**, 1190 (2016).

[27] W. T. Chen, A. Y. Zhu, M. Khorasaninejad, Z. Shi, V. Sanjeev, and F. Capasso, *Immersion Meta-lenses at Visible Wavelengths for Nanoscale Imaging*, Nano Lett. **17**, 3188 (2017).

[28] E. Arbabi, A. Arbabi, S. M. Kamali, Y. Horie, and A. Faraon, *Multiwavelength Polarization-Insensitive Lenses Based on Dielectric Metasurfaces with Meta-molecules*, Optica **3**, 628 (2016).

[29] M. P. Backlund, A. Arbabi, P. N. Petrov, E. Arbabi, S. Saurabh, A. Faraon, and W. E. Moerner, *Removing Orientation-Induced Localization Biases in Single-Molecule Microscopy Using a Broadband Metasurface Mask*, Nat. Photonics **10**, 459 (2016).

[30] F. Ding, Z. Wang, S. He, V. M. Shalaev, and A. V. Kildishev, *Broadband High-Efficiency Half-Wave Plate: A Supercell-Based Plasmonic Metasurface Approach*, ACS Nano **9**, 4111 (2015).

[31] Z. H. Jiang, L. Lin, D. Ma, S. Yun, D. H. Werner, Z. Liu, and T. S. Mayer, *Broadband and Wide Field-of-View Plasmonic Metasurface-Enabled Waveplates*, Sci. Rep. **4**, 7511 (2014).

[32] B. Desiatov, N. Mazurski, Y. Fainman, and U. Levy, *Polarization Selective Beam Shaping Using Nanoscale Dielectric Metasurfaces*, Opt. Express **23**, 22611 (2015).

[33] L. Wang, S. Kruk, H. Tang, T. Li, I. Kravchenko, D. N. Neshev, and Y. S. Kivshar, *Grayscale Transparent Metasurface Holograms*, Optica **3**, 1504 (2016).

[34] S. Choudhury, U. Guler, A. Shaltout, V. M. Shalaev, A. V. Kildishev, and A. Boltasseva, *Pancharatnam-Berry Phase Manipulating Metasurface for Visible Color Hologram Based on Low Loss Silver Thin Film*, Adv. Opt. Mater. **5**, 1700196 (2017).

[35] Y. Ren *et al.*, *Orbital Angular Momentum-Based Space Division Multiplexing for High-Capacity Underwater Optical Communications*, Sci. Rep. **6**, 33306 (2016).

[36] F. Bouchard, I. De Leon, S. A. Schulz, J. Upham, E. Karimi, and R. W. Boyd, *Optical Spin-to-Orbital Angular Momentum Conversion in Ultra-thin Metasurfaces with Arbitrary Topological Charges*, Appl. Phys. Lett. **105**, 101905 (2014).

[37] S. M. Kamali, A. Arbabi, E. Arbabi, Y. Horie, and A. Faraon, *Decoupling Optical Function and Geometrical Form Using Conformal Flexible Dielectric Metasurfaces*, Nat. Commun. **7**, 11618 (2016).

[38] E. Arbabi, A. Arbabi, S. M. Kamali, Y. Horie, and A. Faraon, *Controlling the Sign of Chromatic Dispersion in Diffractive Optics with Dielectric Metasurfaces*, Optica **4**, 625 (2017).

[39] A. Arbabi, E.Arbabi, Y. Horie, S. M. Kamali, and A. Faraon, *Planar Metasurface Retroreflector*, Nat. Photonics **11**, 415 (2017).

[40] A. Silva, F. Monticone, G. Castaldi, V. Galdi, A. Alu, and N. Engheta, *Performing Mathematical Operations with Metamaterials*, Science **343**, 160 (2014).

[41] S. Liu, A. Vaskin, S. Campione, O. Wolf, M. B. Sinclair, J. Reno, G. A. Keeler, I. Staude, and I. Brener, *Huygens' Metasurfaces Enabled by Magnetic Dipole Resonance Tuning in Split Dielectric Nanoresonators*, Nano Lett. **17**, 4297 (2017).

[42] Z. Lin, B. Groever, F. Capasso, A. W. Rodriguez, and M. Lončar, *Topology Optimized Multi-layered Meta-optics*, arXiv:1706.06715.

[43] D. Fattal, J. Li, Z. Peng, M. Fiorentino, and R. G. Beausoleil, *Flat Dielectric Grating Reflectors with Focusing Abilities*, Nat. Photonics **4**, 466 (2010).

[44] S. M. Kamali, E. Arbabi, A. Arbabi, Y. Horie, and A. Faraon, *Highly Tunable Elastic Dielectric Metasurface Lenses*, Laser Photonics Rev. **10**, 1002 (2016).

[45] A. Arbabi, E. Arbabi, S. M. Kamali, Y. Horie, S. Han, and A. Faraon, *Miniature Optical Planar Camera Based on a Wide-Angle Metasurface Doublet Corrected for Monochromatic Aberrations*, Nat. Commun. **7**, 13682 (2016).

[46] R. Paniagua-Dominguez *et al.*, *A Metalens with Near-Unity Numerical Aperture*, arXiv:1705.00895.

[47] Y. Yang, A. E. Miroshnichenko, S. V. Kostinski, M. Odit, P. Kapitanova, M. Qiu, and Y. S. Kivshar, *Multimode Directionality in All-Dielectric Metasurfaces*, Phys. Rev. B **95**, 165426 (2017).

[48] J. R. Ong, H. S. Chu, V. H. Chen, A. Y. Zhu, and P. Genevet, *Freestanding Dielectric Nanohole Array Metasurface for Mid-infrared Wavelength Applications*, Opt. Lett. **42**, 2639 (2017).

[49] A. Arbabi, R. M. Briggs, Y. Horie, M. Bagheri, and A. Faraon, *Efficient Dielectric Metasurface Collimating Lenses for Mid-infrared Quantum Cascade Lasers*, Opt. Express **23**, 33310 (2015).

[50] S. Colburn, A. Zhan, and A. Majumdar, *Tunable Metasurfaces via Subwavelength Phase Shifters with Uniform Amplitude*, Sci. Rep. **7**, 40174 (2017).

[51] J. Yang and J. A. Fan, *Topology-Optimized Metasurfaces: Impact of Initial Geometric Layout*, Opt. Lett. **42**, 3161 (2017).

[52] Z. Zhou *et al.*, *Efficient Silicon Metasurfaces for Visible Light*, ACS Photonics **4**, 544 (2017).

[53] M. Parry, A. Komar, B. Hopkins, S. Campione, S. Liu, A. E. Miroshnichenko, J. Nogan, M. B. Sinclair, I. Brener, and D. N. Neshev, *Active Tuning of High-Q Dielectric Metasurfaces*, Appl. Phys. Lett. **111**, 053102 (2017).

[54] K. Li, C. Chase, P. Qiao, and C. J. Chang-Hasnain, *Widely Tunable 1060-nm VCSEL with High-Contrast Grating Mirror*, Opt. Express **25**, 11844 (2017).

[55] A. Forouzmand and H. Mosallaei, *All-Dielectric C-Shaped Nanoantennas for Light Manipulation: Tailoring Both Magnetic and Electric Resonances to the Desire*, Adv. Opt. Mater. **5**, 1700147 (2017).

[56] E. Maguid, I. Yulevich, M. Yannai, V. Kleiner, M. L Brongersma, and E. Hasman, *Multifunctional Interleaved Geometric Phase Dielectric Metasurfaces*, Light Sci. Appl. **6**, e17027 (2017).

[57] A. Di Falco, Y. Zhao, and A. Alú, *Optical Metasurfaces with Robust Angular Response on Flexible Substrates*, Appl. Phys. Lett. **99**, 163110 (2011).

[58] Q. Zheng *et al.*, *Wideband, Wide-Angle Coding Phase Gradient Metasurfaces Based on Pancharatnam-Berry Phase*, Sci. Rep. **7**, 43543 (2017).

[59] M. Born, E. Wolf, and A. Bhatia, *Principles of Optics: Electromagnetic Theory of Propagation, Interference and Diffraction of Light* (Cambridge University Press, Cambridge, England, 1999).

[60] R. C. Fairchild and J. R. Fienup, *Computer-Originated Aspheric Holographic Optical-Elements*, Opt. Eng. (Bellingham, Wash.) **21**, 211133 (1982).

[61] M. Jang *et al.*, *Complex Wavefront Engineering with Disorder-Engineered Metasurfaces*, arXiv:1706.08640.

[62] S. Feng, C. Kane, P. A. Lee, and A. D. Stone, *Correlations and Fluctuations of Coherent Wave Transmission through Disordered Media*, Phys. Rev. Lett. **61**, 834 (1988).

[63] See Supplemental Material at http://link.aps.org/supplemental/10.1103/PhysRevX.7.041056 for simulation details and measurement setups.

[64] A. F. Oskooi, D. Roundy, M. Ibanescu, P. Bermel, J. D. Joannopoulos, and S. G. Johnson, *MEEP: A Flexible Free-Software Package for Electromagnetic Simulations by the FDTD Method*, Comput. Phys. Commun. **181**, 687 (2010).

[65] J. Cheng, S. Inampudi, and H. Mosallaei, *Optimization-Based Dielectric Metasurfaces for Angle-Selective Multifunctional Beam Deflection*, Sci. Rep. **7**, 12228 (2017).

[66] V. S. Asadchy, A. Diaz-Rubio, S. N. Tcvetkova, D. H. Kwon, A. Elsakka, M. Albooyeh, and S. A. Tretyakov, *Flat Engineered Multichannel Reflectors*, Phys. Rev. X **7**, 031046 (2017).

[67] J. P. Balthasar Mueller, N. A. Rubin, R. C. Devlin, B. Groever, and F. Capasso, *Metasurface Polarization Optics:*

Independent Phase Control of Arbitrary Orthogonal States of Polarization, Phys. Rev. Lett. **118**, 113901 (2017).

[68] F. Aieta, M. A. Kats, P. Genevet, and F. Capasso, *Multiwavelength Achromatic Metasurfaces by Dispersive Phase Compensation*, Science **347**, 1342 (2015).

[69] E. Arbabi, A. Arbabi, S. M. Kamali, Y. Horie, and A. Faraon, *Multiwavelength Metasurfaces through Spatial Multiplexing*, Sci. Rep. **6**, 32803(2016).

[70] D. Lin, A. L. Holsteen, E. Maguid, G. Wetzstein, P. G. Kik, E. Hasman, and M. L. Brongersma, *Photonic Multitasking Interleaved Si Nanoantenna Phased Array*, Nano Lett. **16**, 7671 (2016).

[71] V. Liu and S. Fan, *S4: A Free Electromagnetic Solver for Layered Periodic Structures*, Comput. Phys. Commun. **183**, 2233 (2012).